Multi-Axis Force Sensing in Laparoscopic Surgery

Amir Hossein Hadi Hosseinabadi , David G. Black , and Septimiu E. Salcudean

Abstract—**This letter presents a novel approach to multi-axis force-sensing in laparoscopic surgery. It requires no modification to the surgical instrument and is therefore adaptable to different surgical tools. The sensing approach relies on a novel cannula design and utilizes a very high-resolution transducer for deflection measurement at the proximal shaft of the surgical instrument. The proposed cannula has an inner tube and an outer tube; the inner tube is attached to the cannula's interface to the robot frame through a compliant leaf spring with adjustable stiffness. It allows bending of the instrument shaft due to the tip forces. The outer tube mechanically filters out the body forces so they do not affect the instrument's bending behavior. An optical transducer with integrated electronics was mounted onto the proximal shaft of a da Vinci EndoWrist. A mathematical model of the sensing system was developed. A setup was built for calibration and testing, and its hardware and software are discussed in detail. Model-based and data-driven calibration approaches were compared. Comprehensive testing was conducted to validate that the sensor can successfully measure the lateral forces and moments and the axial torque applied to the instrument's distal end within the desired resolution, accuracy, and range requirements.**

Index Terms—**Haptics and haptic interfaces, surgical robotics - laparoscopy, force and tactile sensing, telerobotics and teleoperation, DVRK.**

I. INTRODUCTION

A. Background

WITH the rapid developments in the fields of robotics, computer vision, and data-driven learning, Robot-Assisted Minimally Invasive Surgery (RAMIS) has been showing exponential growth over the past decade [1]. However, the clinical systems do not provide haptic perception [2] depriving the surgeon of the rich information embedded in palpating the tissue. Recent surveys [3], [4] show that haptic perception is proven to decrease operation time, facilitate training, improve accuracy, and enhance patient safety. Any haptic interface requires a method of force sensing.

Strain gauges, capacitive, and optical transducers have been integrated into the instrument's base [5], proximal and distal shaft [6], [7], wrist [8], [9], cannula [10], and gripper [11],

[12]. Micro-Electro-Mechanical (MEM) fabrication techniques have also been used to develop cost-effective, compact, fully-integrated, and monolithic sensors [13]. However, most of the listed literature requires modifications to the instrument. Thus, the concepts surveyed above are limited to one instrument type that leads to increased design, fabrication, and maintenance costs [14]. Jones et al. [15] and Spiers et al. [16] integrated custom strain-gauge torque sensors at the mounting interface of the EndoWrist instruments. A model of the cable drive train was used to calculate the forces applied to the gripper. Wang et al. [17] used strain gauges in a custom cover plate at the instrument interface, and the docking clamps that hold the cannula to measure the axial and lateral forces, respectively. Ranzani et al. [18] designed two custom holders, for an endo-lumnial instrument and the fulcrum point, with integrated ATI F/T sensors. Kim et al. [19] replaced the cannula's support with a 3-axis I-Beam force sensor using strain-gauges to measure the instrument's lateral forces. Fontanelli et al. [20] used four optical proximity sensors in an instrumented cannula to measure the deflection of the instrument shaft. The proposed concept was able to measure the lateral forces with no instrument modification. However, the sensor needs to be in the abdominal cavity, and the size of the access hole has to be larger than the cannula.

As a result, there remains a need for a complete force sensing solution with real research and clinical utility. In [21], we validated the feasibility of a novel optical sensor, though it was limited to lateral forces in an ideal setting without nonlinear boundary conditions (e.g. instrument insertion into the cannula). In this letter, we extend our previous work to offer an adaptable solution for multi-axis force sensing in robotic laparoscopic surgery, using the da Vinci EndoWrist, without modifying the surgical instrument.

B. Design Objectives

Multi-axis: The literature suggests that the lateral forces should be the primary focus for an effective haptic experience, and the axial force and moment are secondary [16].

Resolution: The human just-noticeable difference (JND) is 10% in the range of 0.5 to 200 N increasing to 15–27% below 0.5 N, which can be considered as a requirement on the sensor accuracy [19]. A resolution of 0.2 N over a range of ± 10 N is suggested for the lateral forces [6]. To the best of our knowledge, no requirements for the other degrees of freedom (DoFs) have been specified.

Sterilizability: The closer the sensor is to the instrument tip, the more stringent the requirements on sterilizability and biocompatibility are. However, mounting the sensor far from the instrument tip raises challenges in sensing accuracy.

Disposability: The da Vinci instruments are disposed after 10 to 15 uses due to accelerated cable fatigue [22]. The EndoWrist instruments retail at $2k-$5k [16]. If the sensor is to be disposed with the instrument, it should not increase the instrument price significantly. An adaptable solution that can be easily used on different instruments is desirable.

C. Contributions

The specific contributions presented in this letter are:
1) We present a continuum mechanics model that explains the bending and axial deflection, as well as the axial torsion of the instrument's shaft considering the varying stiffness at the cannula due to instrument insertion.
2) We propose a novel two-layer compliant cannula to mechanically filter out the access port forces. This solution is light-weight, does not modify the instrument-robot mounting interface, and extends the range over which the instrument's bending behavior is linear.
3) We developed a calibration setup that easily integrates into the dVRK [23] platform and accommodates repeatable calibration over the instrument's entire stroke.
4) We adopted a system identification approach for sensor calibration, and compared it against a data-driven (shallow neural-network) calibration approach.
5) Lastly, we experimentally validated the effectiveness of the new cannula design in filtering out the body-wall disturbance forces, and quantified the force artifacts due to the instrument's wrist actuation.

II. SENSING APPROACH AND TWO-LAYER CANNULA

A force sensor that can be mounted onto the distal shaft can be adaptable to different instrument types with more relaxed requirements for use in a clinical setting. Force sensing at the distal shaft relies on using transducers that can measure small deflections of the instrument shaft due to the wrench vector applied at its tip. These deflections are in the order of a few microns. Thus our earlier effort published in [24] was focused on developing a multi-axis force sensor with sub-nanometer resolution in displacement measurement using bicell photodiodes. The sensor has a hole in its central axis about which six optical transducers are mounted in a hexagonal arrangement. Each optical transducers can provide Ångström level resolution in deflection measurement.

In addition to small deflections, force sensing at the proximal shaft may be affected by disturbance forces between the cannula and the patient's body [25]. To address this, we modified the cannula in the da Vinci classic system. The instrument now passes through an inner tube covered by an outer tube, with a 0.5 mm air gap on each side (see Fig. 1). This design is referred to as the "two-layer" cannula. The outer tube, in contact with the patient's body, is rigidly attached to the robot frame. Consequently, body wall forces are directly transferred to the robot frame, mechanically filtering them from the inner tube and the surgical instrument.

As shown in Figs. 1 and 3, the inner tube is connected to the cannula's base via a custom leaf spring. Lateral forces on the
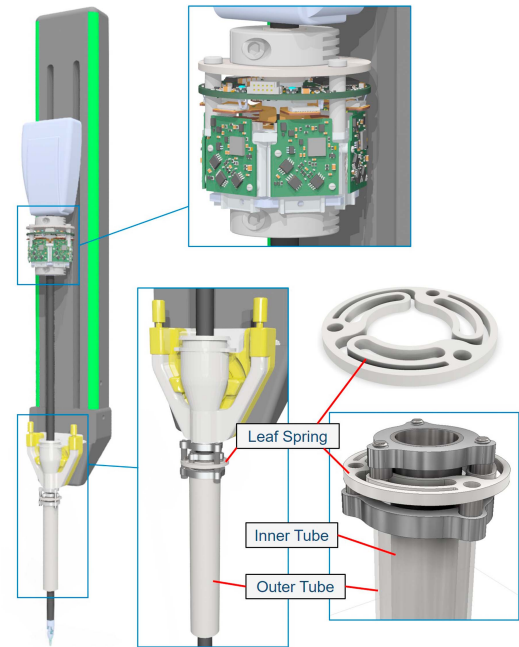

Fig. 1.   6-axis optical force sensor mounted onto the proximal shaft and two-layer Cannula design.
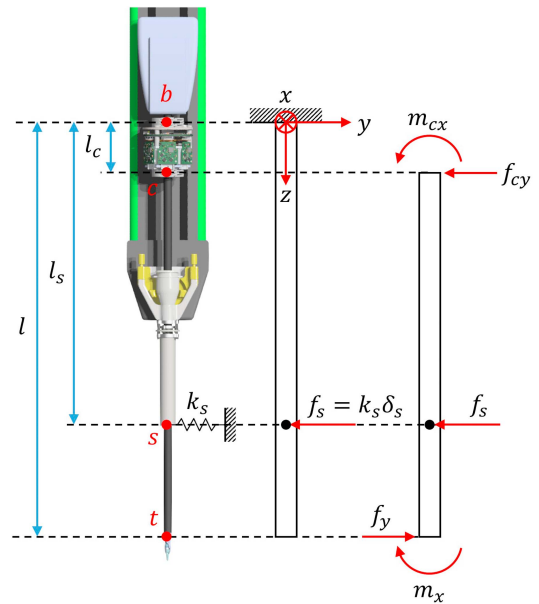

Fig. 2.   Schematic for the instrument's bending model.

instrument pivot the inner tube, reducing its air gap to the outer tube. The leaf spring is designed to provide 20 N/mm equivalent stiffness at the tip of the inner tube; at the maximum lateral force of ±10 N, the inner tube's tip displacement does not close the aforementioned 0.5 mm air gap. It's stiffness is tuned by three axis-symmetric arms and arc-shaped slots. After stiffness tuning, having it adjustable is not a requirement for clinical deployment.
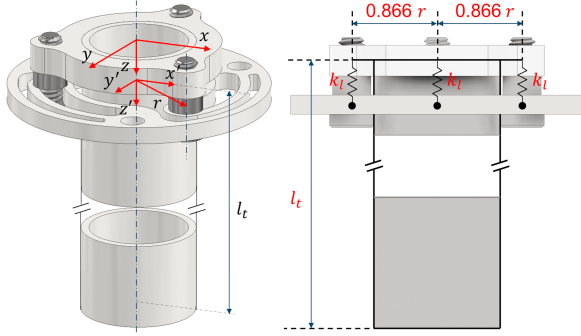
Fig. 3. Schematic of the equivalent stiffness at the distal end of the inner tube as a function of the leaf-spring's parameters.

III. MODELING

The bending behavior of the instrument's shaft changes by its insertion lengths into the cannula. A mathematical model from the forces and moments at the distal end of the instrument shaft (point t in Fig. 2) to the transducers signals of the optical force sensor was developed. From [24] The sensor's response to a wrench vector applied at its clamping point (point c) is explained by:

$$\vec{n} = C_m \vec{w}_c \qquad (1)$$

where $\vec{w}_c = [f_{cx}, f_{cy}, f_{cz}, m_{cx}, m_{cy}, m_{cz}]^T$ is the wrench vector at point c, $\vec{n} = [n_1, \ldots, n_6]^T$) is the vector of transducers signals, and C_m is a calibration matrix.

Equations (2) to (4) model the reflected wrench vector at the shaft's cross-section at point c as a function of the wrenches applied at the point t ($\vec{w}_t = [f_x, f_y, f_z, m_x, m_y, m_z]^T$) considering the change in the instrument's insertion into the cannula (l_s). l, l_s, and l_c are the distances from the shaft's distal end (t), the cannula's distal end (s), and the clamping point of the passive component (c), to the upper clamping point of sensor (b), respectively (see Fig. 2). The parameter l_s is of particular importance to model since the sensing is strongly affected by the insertion depth of the surgical instrument, which changes frequently.

$$\vec{w}_c = H_c \vec{w}_t$$

$$H_c = \begin{bmatrix} H_{11} & 0 & 0 & 0 & -3g(\kappa_y) & 0 \\ 0 & H_{22} & 0 & 3g(\kappa_x) & 0 & 0 \\ 0 & 0 & 1 & 0 & 0 & 0 \\ 0 & H_{42} & 0 & H_{44} & 0 & 0 \\ H_{51} & 0 & 0 & 0 & H_{55} & 0 \\ 0 & 0 & 0 & 0 & 0 & 1 \end{bmatrix}$$

$$\begin{cases} H_{11} = 1 - (3l - l_s)g(\kappa_y) \\ H_{22} = 1 - (3l - l_s)g(\kappa_x) \\ H_{42} = (3l - l_s)(l_s - l_c)g(\kappa_x) - (l - l_c) \\ H_{44} = 1 - 3(l_s - l_c)g(\kappa_x) \\ H_{51} = (l - l_c) - (3l - l_s)(l_s - l_c)g(\kappa_y) \\ H_{55} = 1 - 3(l_s - l_c)g(\kappa_y) \end{cases}$$

$$g(x) = \frac{l_s^2}{x + 2l_s^3}, \kappa_x = \frac{6EI_{xx}}{k_s}, \kappa_y = \frac{6EI_{yy}}{k_s}. \qquad (2)$$

In (2), k_s is the cannula's equivalent stiffness at its distal end, which is a function of the stiffness of the leaf bearing's arms (k_l) as given in (3). r is the radius of the circle passing through the centerlines of the flexible arms and l_t is the length of the cannula's inner tube as shown in Fig. 3.

$$k_s = \frac{2r}{l_t} k_l \qquad (3)$$

k_l is a function of the thickness of the spring-steel sheet, the effective length of the flexible arms, and the width of the pocketed slot. With a simplified beam bending model, k_l can be approximated as:

$$k_l = \frac{3E_s I_s}{l_e^3}, \qquad (4)$$

where $I_s = \frac{1}{12}(d_o - d_i)h^3$ with d_o as the width of the arm and d_i as the width of the center slot, h and E_s are the thickness and the modulus of elasticity of the spring-steel sheet, respectively, and l_e is the effective length of the arms. The stiffness of the flexible arms can be uniformly adjusted by rotating the inner tube and consequently changing l_e. Combining (1) and (2), the mapping from the applied wrench at the distal end of the instrument to the sensor signals is:

$$\vec{n} = C_m H_c \vec{w}_t. \qquad (5)$$

IV. CALIBRATION

A. Hardware and Software

Fig. 4 shows the optical transducers mounted onto the proximal shaft of the ProGrasp instrument, and the modified cannula. This instrument features a wrist design at the distal shaft similar to that of many common surgical instruments in daVinci, RAVEN, and other RMIS systems. Its use is representative of the most common surgical instruments and aligns with current practices in the literature [14]. A calibration setup (see Fig. 6) was designed to measure the sensor signals throughout its insertion stroke while 6-axis forces and moments are applied to the distal end of the instrument shaft. It has a linear stage (T-LSR150B from Zaber Technologies, Canada) that moves synchronously with the nominal insertion axis (q_{3n}) of the patient side manipulator (PSM), and an ATI Nano43 Force-Torque (F/T) sensor as the reference. The ATI sensor is clamped to the instrument's distal shaft and attached to 3 equally-spaced radial elastic bands. The relative motion of the instrument with respect to the linear stage stretches at least one of the bands; their combination applies forces and moments to the instrument's shaft.

Fig. 5 shows a block diagram of the calibration hardware and its software architecture. The connection with the Power/Com board, that samples all the optical transducers, and the linear stage are via USB high-speed to RS485 (FT2232H from Future Technology Devices International (FTDI)) and RS232 (T-USBDC from Zaber Technologies) bridges, respectively. The ATI F/T sensor is interfaced to the calibration PC through a data acquisition card (PCI-6220 M series, National Instruments).

(b) 6-Axis force sensor

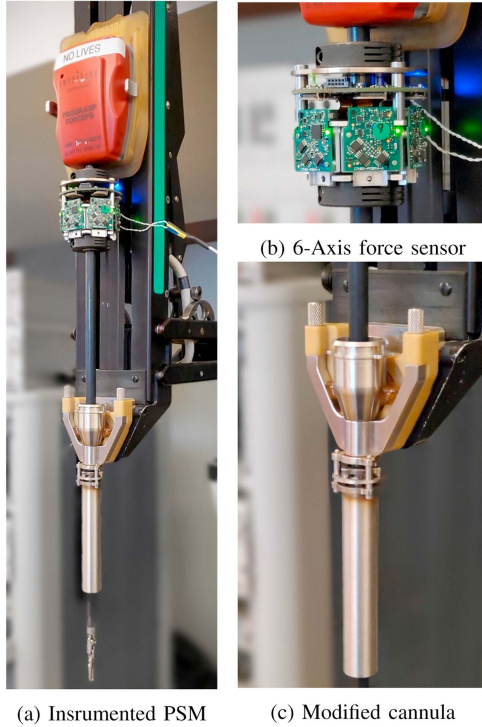(a) Insrumented PSM   (c) Modified cannula

Fig. 4.   The 6-axis optical force sensor mounted onto the instrument. The original cannula of the standard daVinci system is replaced by the modified cannula.

The interface with the da Vinci PSM is through an IEEE-1394a FireWire port (TSB12LV23, Texas Instruments).

A Python library (*sensor.py*) was developed to interface with the Power/Com board to configure the LEDs' forward currents and read the sampled differential and common-mode signals. It uses *pylibftdi*; a thin wrapper over *libftdi* that is an open source C/C++ FTDI driver library for transactions over the USB-RS485 bridge. Another Python library (*ati.py*) was developed to read the ATI F/T signals and resolve the reference wrench vector after bias-correction and applying the calibration matrix. It uses *comedilib* to manage transactions over the NI DAQ card. The da Vinci PSM was controlled via the da Vinci Research Kit (dVRK) [23]; an open-source mechatronics system to control research systems based on the retired first-generation da Vinci system. It has libraries in Python (dVRK-Python) and MATLAB (dVRK-MATLAB) to control the PSM and access its joints parameters.

The calibration software was developed using the Robot Operating System (ROS) framework. When launched, it creates three rosnodes; Logger, Planner, and Stage. The Planner node generates random motion trajectories along the stroke of the PSM's insertion axis (see Sections IV-B and IV-C). The Stage node initializes the linear stage and follows the nominal position of the PSM's insertion joint (q_{3n}). The Logger node records the optical transducers' signals, the ATI reference measurements, and the joints positions of the da Vinci PSM. Rostopics were used for communication and handshaking between the rosnodes. The calibration software and the dVRK app run on Ubuntu 18.04 operating system.

B. Model-Based Calibration

In our first attempt, the model developed in Section III was used for sensor calibration. The instrument was moved axially (q_3) throughout its stroke with sequentially random axial and lateral motions and axial rotation about its shaft (q_4). Fig. 7 shows the motion profiles. The calibration trajectory was designed to respect the robot's velocity limits, preventing unmodeled dynamics due to actuators' saturation. Additionally, it aimed to impose single-axis loading, minimizing cross-coupling and ensuring the validity of the assumptions made in Section III for the developed model. Two data-collection cycles were executed. The first cycle was used for calibration, and the second cycle was used for testing. MATLAB's constrained optimization toolbox was used to fit a model described by (5) to the measurements. The constraints in (6) were defined. c_{xn} and c_{yn} are the nominal estimations by using (2). Given that l_s decreases as the instrument penetrates into the cannula, it was reformulated as $l_s = l_{os} - q_3$ where l_{os} is an offset value. l_c was set to 0.035 m that is the distance between points b and c (Fig. 2).

$$\begin{cases} 0 < \kappa_x < 2c_{xn} \\ 0 < \kappa_y < 2c_{yn} \\ l_c < l_s < l \\ 0 < l < 0.50m \end{cases}, \tag{6}$$

Fig. 8 shows the calibration results. The optical transducers can closely reconstruct the wrench vector in all the DoFs, except the axial force; it is because the axial force is affected by the friction between the instrument and the cannula when lateral forces and moments exist. Additionally, the model-based calibration is valid only for the scenarios where the modeling assumptions are valid. Fig. 9 further elaborates on this; 1) when the moment is small, and no lateral force is applied, the deformed shape of the instrument makes no contact with the inner tube; therefore, the cannula stiffness is zero, 2) when the moment is large, the instrument hits the walls of the inner tube in addition to its tip; thus making two contact points with the cannula and the model invalid. When insertion depth is large, the supported end of the instrument is closer to the cannula, so the first scenario with small bending is more likely. Conversely, when the insertion depth is small, the latter is more likely.

C. Data-Driven Calibration

A data-driven calibration was developed to address the shortcomings of the model-based calibration. Here, supervised learning techniques, e.g. neural networks, are adopted to identify a mapping between the sensor signals and the reference measurements. Compared to a model-based calibration, a data-driven approach is more powerful in compensating for the unmodeled dynamics, e.g. friction, backlash, hysteresis, changing dynamics, and other system nonlinearities. Thus, the calibration trajectory, as shown in Fig. 10, was less constrained. Considering the robot's velocity limits, the instrument was randomly moved for 10 cycles in a traveling 40 mm cube along the insertion axis
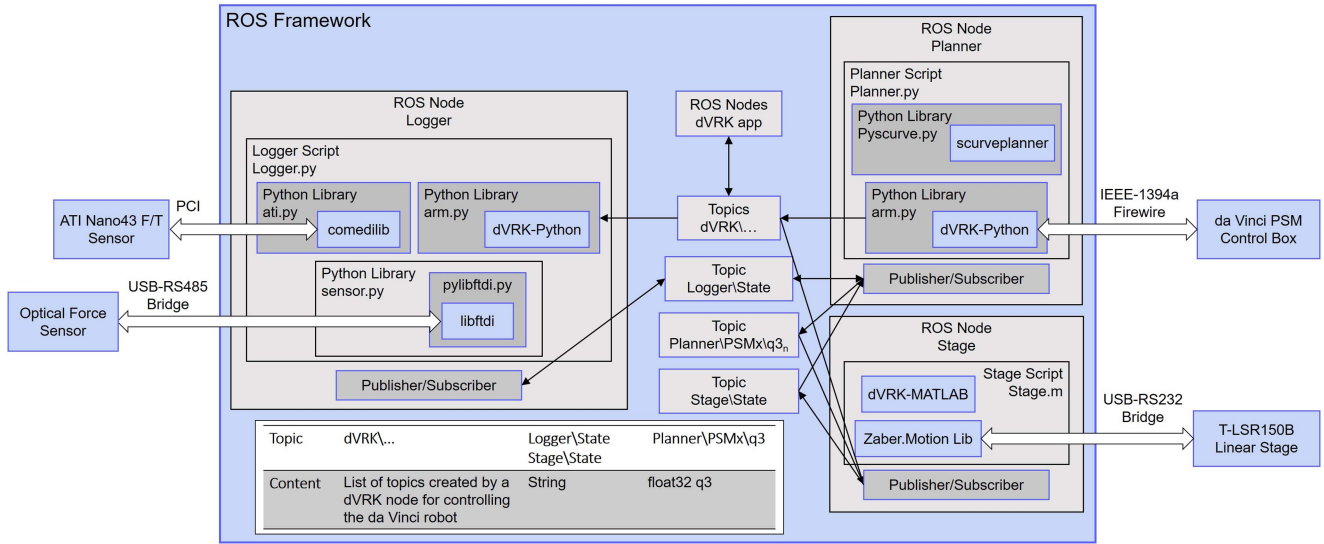
Fig. 5. Block diagram of the calibration setup; hardware and software.
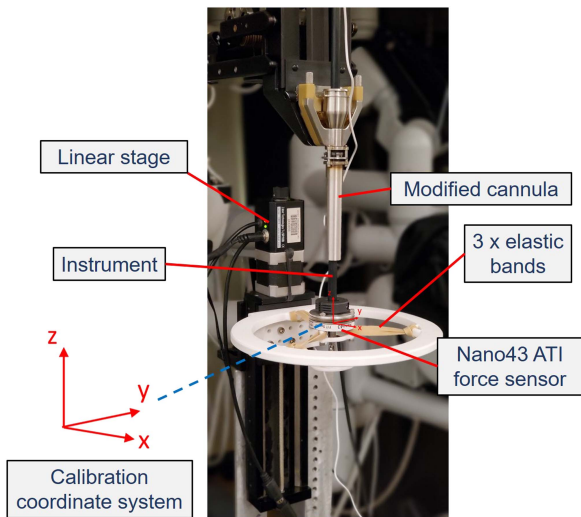

Fig. 6. Calibration setup has a linear stage that moves in sync with the insertion axis of the PSM.
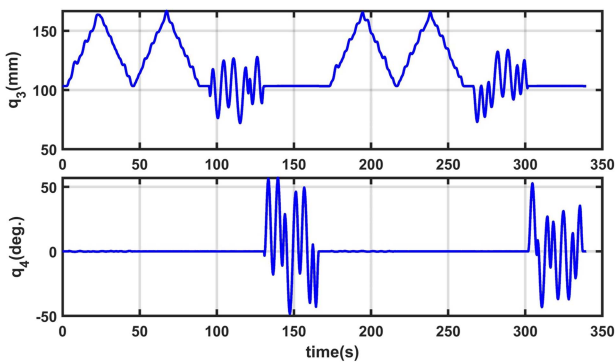

Fig. 7. Instrument's displacement profile along the insertion axis (q_3) and axial rotation (q_4) in model-based calibration.
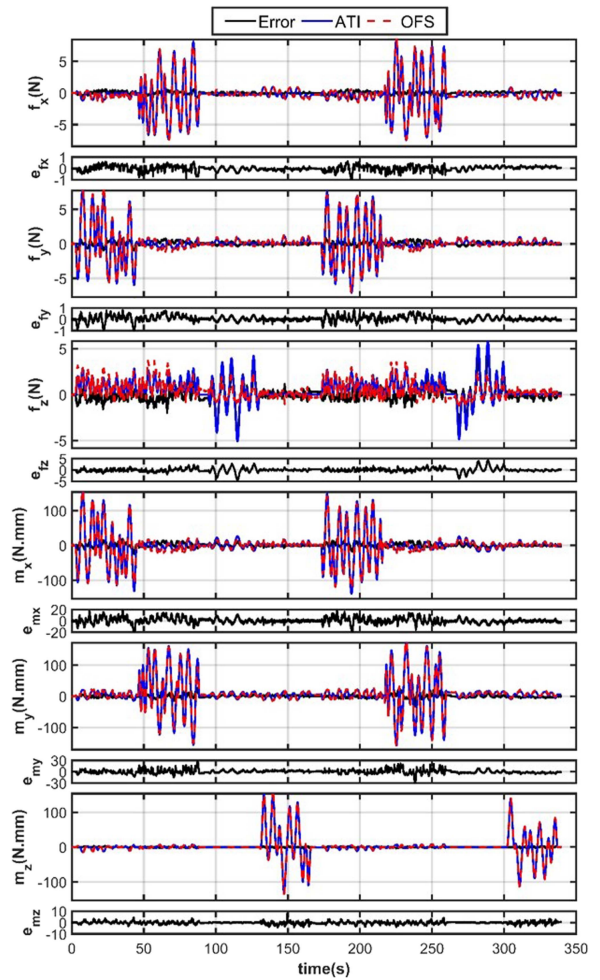

Fig. 8. Model-based calibration: Force applied at the distal end of the instrument's shaft vs the calibrated optical force sensor mounted onto its proximal shaft.
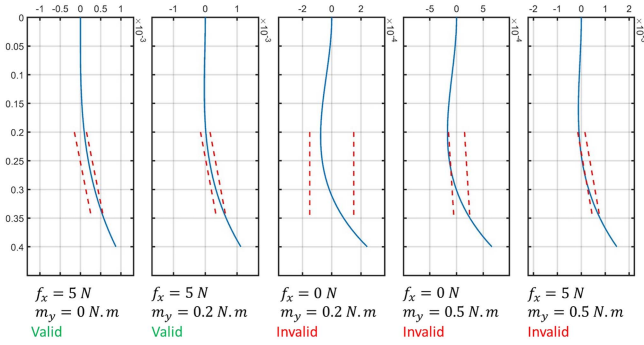
Fig. 9. Dashed red line: cannula's inner tube. Blue line: bending profile of the instrument's shaft's. This figure shows the scenarios where the model in (5) is valid.
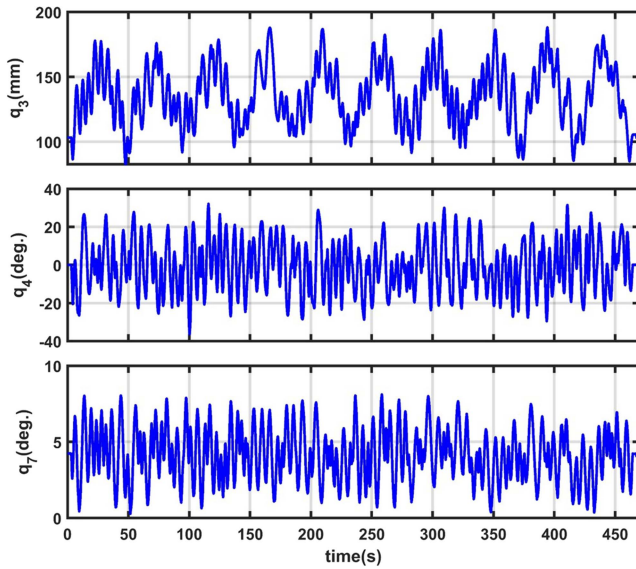

Fig. 10. Instrument's displacement profile along the insertion axis (q_3), axial rotation (q_4), and gripper angle (q_7) in data-driven calibration.
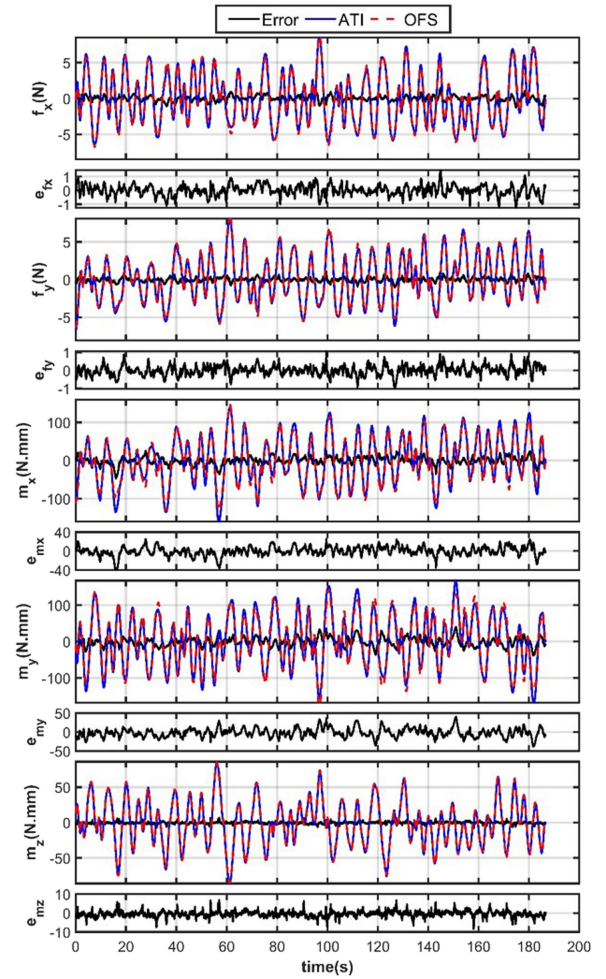

Fig. 11. Data-driven calibration results: force applied at the distal end of the instrument's shaft vs the calibrated optical force sensor mounted onto its proximal shaft.

of the PSM. Additionally, A compressible foam was placed between the grippers and the gripper angle was randomly changed between 0 (firm grip) and 9 (loose grip) degrees.

MATLAB's FitNet nonlinear regression tool was used for training different neural network architectures. A 2-layer neural network, with 5 nodes in the hidden layer and 5 nodes in the output layer, was found to fit the validation set without overfitting the training data. The input layer is a 15×1 vector as given in (7) where q_3 and q_4 are the PSM's insertion in mm and axial rotation in rad., respectively, m_g is the jaw effort in N · mm, and n_i are the transducers signals. The jaw effort was added to compensate for the induced forces in the shaft when the instrument firmly grasps an object.

$$ x_{in} = \left[q_3, q_4, m_g, n_1, \ldots, n_6, n_1^2, \ldots, n_6^2 \right]^T \qquad (7) $$

Fig. 11 shows that the calibrated sensor closely resolves the forces measured by the reference sensor. It is important to note that, in the data-driven calibration, the effect of the jaw effort on the sensor readings is compensated by including the jaw effort

in the network's input vector. It is much more complex to model and to compensate for in the model-based calibration. The performance of the NN architecture was quantified in different axes and is compared with the model-based calibration in Table I. As

TABLE I
COMPARISON OF THE ERROR (e_i) STATISTICS (σ_i AND NRMSD$_i$) AND SENSOR LINEARITY (R_i^2) FOR MODEL-BASED AND DATA-DRIVEN CALIBRATION SCHEMES

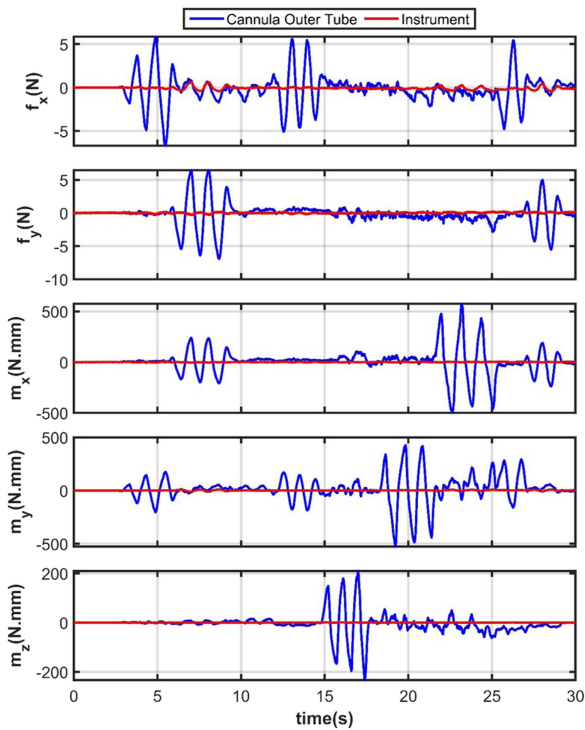| Axis		f_x	f_y	m_x	m_y	m_z
Unit		N	N	N·mm	N·mm	N·mm
i		1	2	4	5	6
Range		±9	±9	±160	±160	±100
σ_i	NN	0.38	0.30	9.43	12.51	2.15
	model	1.08	0.97	16.74	23.16	2.36
NRMSD$_i$(%)	NN	0.80	1.02	0.92	0.95	0.21
	model	7.52	7.63	6.50	7.39	1.51
R_i^2 (dmls)	NN	0.98	0.98	0.97	0.97	0.99
	model	0.89	0.86	0.89	0.88	0.99

Fig. 12. Overcoat test - The ATI sensor was attached to the outer tube of the cannula and the sensor signals are resolved using the calibration neural network to identify the effect of the body wall forces.

it can be seen, the NN outperforms the model-based calibration in all the axes.

V. DESIGN EVALUATION

A. Overcoat Test

The overcoat test was performed to evaluate whether the proposed cannula design is effective in filtering the forces applied to its outer tube. The ATI sensor was attached to the cannula's outer tube via a 3D-printed adapter, and sequences of forces and moments were applied to it. As shown in Fig. 12, despite the relatively large forces and moments applied to the cannula's outer tube, the optical force sensor picks up minor oscillations in the resolved wrench vector. Hence, the cannula's two-layer design effectively filters out the body forces from the sensor readings.

B. Wrist Maneuver Test

The wrist maneuver test was performed to evaluate the effect of wrist motions on forces generated in the instrument shaft. The wrist was sequentially moved between its mechanical limits in the pitch (q_5) and yaw (q_6) axes, and the gripper was fully opened and closed (q_7) as shown in the top plot of Fig. 13. The gripper was commanded to -10° to generate a grasping force in the closed state. The two bottom plots show the forces and moments in the instrument shaft measured by the optical force sensor and the data-driven calibration pipeline (see Section IV-C). The plots
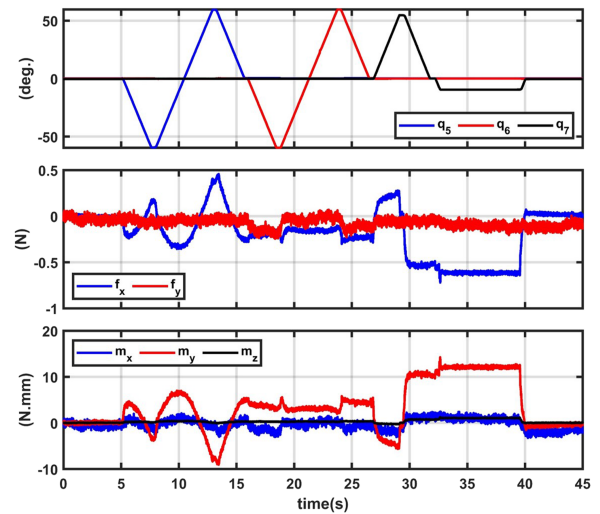

Fig. 13. Wrist maneuver test - The instrument's wrist was moved within its mechanical range and the induced forces in the instrument shaft was estimated using the data-driven calibration pipeline.

show that the wrist motions and the gripper forces have minimal effect on the f_y, m_x, and m_z. However, they have a noticeable effect on the f_x, and m_y components. Considering the range and the RMS values in Table I, the contribution of the wrist maneuvers and grasping forces on the measurements are within the $2\sigma_i$ error margin. Without having the jaw effort (m_g) in the network inputs, the errors due to the wrist actuation could be as large as $20\sigma_i$.

VI. DISCUSSION AND CONCLUSION

In this letter, we proposed a novel adaptable approach comprising a high-resolution optical sensor and a two-layer cannula design to measure the lateral forces and moments applied at the distal end of laparoscopic instruments. This idea can be easily applied to the standard da Vinci cannula's as well as the AirSeal access ports from CONMED [26] for reduced friction.

A mathematical model, developed to capture changes in the instrument's bending behavior during its insertion into the cannula, served both for model-based calibration and design trade-off evaluations. Calibration results demonstrated the model's ability to capture dynamics under varying boundary conditions. However, experimentation with various system identification algorithms revealed its limitations in explaining nonlinear dynamics during multi-axis force applications. The drawbacks of model-based calibration were discussed in Section IV-B and compared to a data-driven approach, which effectively handles unmodeled scenarios and compensates for the complex-to-model effect of grasping force on measurements. The data-driven approach improved the NRMSD by a factor of 7–10 compared to the model-based approach.

The data-driven calibration results showed an accuracy of close to 10% in the lateral forces, which is the human's JND over the range of 0.5–200 N as explained in Section I. As expected, the best accuracy ($\sim$6%) was obtained in the axial torque. This

is because the sensor configuration is most sensitive to the axial torque and it is not affected by the changes in the instrument support (see (1) and (2)). Thus, the design meets the design objectives in terms of resolution and is acceptable for use in research RAMIS platforms in all but the axial force. Despite the high-resolution displacement measurement that the sensor provides, it failed to closely resolve the axial force.

As mentioned in Section I, the axial force is least important to capture accurately [16]. Nevertheless, future work will focus on improving this aspect of the calibration. Design modifications such as using the AirSeal access port, and adding a Teflon coating or bronze bushings at the tip of the cannula's inner tube can improve the sensor performance in the axial direction by reducing the friction. Moreover, in the future, we will focus on cascading a supervised learning calibration designed to reconstruct the axial force components without degrading the sensor performance in the other DoFs.

The overcoat test and the wrist maneuver test were conducted to further evaluate the proposed sensing approach. The former showed that the modified cannula can properly filter the body wall forces from the measurements. The latter verified that the grasping forces have a more dominant effect on the measurement accuracy compared to the wrist actuation in the pitch and yaw axes.

Despite the advantages noted above, our sensing approach also has limitations. In particular, (i) The calibration needs to be repeated after every sensor installation onto the PSM; in the future, a mechanical references can be added for a more accurate positioning and repeatable sensor installation which could eliminate the need for re-calibration, and (ii) The current sensor needs another reference sensor and the calibration setup in Section IV for calibration. In future work, we plan to explore other calibration methods that do not rely upon an external sensor, e.g., using the IMU and the inertial parameters of a known payload, or by payload estimation.

ACKNOWLEDGMENT

REFERENCES

[1] Intuitive Surgical Inc. J.P. Morgan Healthcare Conference, 2021, Accessed: Mar. 10, 2021. [Online]. Available: https://isrg.intuitive.com/

[2] A. Abiri et al., "Visual–Perceptual mismatch in robotic surgery," *Surg. Endoscopy*, vol. 31, no. 8, pp. 3271–3278, Aug. 2017.

[3] I. El Rassi and J. M. El Rassi, "A review of haptic feedback in tele-operated robotic surgery," *J. Med. Eng. Technol.*, vol. 44, pp. 247–254, Jul. 2020.

[4] K. Rangarajan, H. Davis, and P. H. Pucher, "Systematic review of virtual haptics in surgical simulation: A valid educational tool?," *J. Surg. Educ.*, vol. 77, no. 2, pp. 337–347, Mar. 2020.

[5] M. Tavakoli, R. V. Patel, and M. Moallem, "Haptic interaction in robot-assisted endoscopic surgery: A sensorized end-effector," *Int. J. Med. Robot. Comput. Assist. Surg.*, vol. 1, no. 2, pp. 53–63, 2005.

[6] A. L. Trejos, A. Escoto, M. D. Naish, and R. V. Patel, "Design and evaluation of a sterilizable force sensing instrument for minimally invasive surgery," *IEEE Sensors J.*, vol. 17, no. 13, pp. 3983–3993, Jul. 2017.

[7] K. S. Shahzada, A. Yurkewich, R. Xu, and R. V. Patel, "Sensorization of a surgical robotic instrument for force sensing," in *Proc. SPIE*, vol. 9702, pp. 153–162, 2016.

[8] D. H. Lee, U. Kim, T. Gulrez, W. J. Yoon, B. Hannaford, and H. R. Choi, "A laparoscopic grasping tool with force sensing capability," *IEEE/ASME Trans. Mechatronics*, vol. 21, no. 1, pp. 130–141, Feb. 2016.

[9] R. Haslinger, P. Leyendecker, and U. Seibold, "A fiberoptic force-torque sensor for minimally invasive robotic surgery," in *Proc. IEEE Int. Conf. Robot. Automat.*, 2013, pp. 4390–4395.

[10] N. Zemiti, G. Morel, T. Ortmaier, and N. Bonnet, "Mechatronic design of a new robot for force control in minimally invasive surgery," *IEEE/ASME Trans. Mechatronics*, vol. 12, no. 2, pp. 143–153, Apr. 2007.

[11] U. Kim, D. H. Lee, W. J. Yoon, B. Hannaford, and H. R. Choi, "Force sensor integrated surgical forceps for minimally invasive robotic surgery," *IEEE Trans. Robot.*, vol. 31, no. 5, pp. 1214–1224, Oct. 2015.

[12] P. Soltani-Zarrin, A. Escoto, R. Xu, R. V. Patel, M. D. Naish, and A. L. Trejos, "Development of a 2-DOF sensorized surgical grasper for grasping and axial force measurements," *IEEE Sensors J.*, vol. 18, no. 7, pp. 2816–2826, Apr. 2018.

[13] Y. Dai et al., "Grasper integrated tri-axial force sensor system for robotic minimally invasive surgery," in *IEEE 39th Proc. Annu. Int. Conf. Eng. Med. Biol. Soc.*, 2017, pp. 3936–3939.

[14] A. H. H. Hosseinabadi and S. E. Salcudean, "Force sensing in robot-assisted keyhole endoscopy: A systematic survey," *Int. J. Robot. Res.*, vol. 41, no. 2, pp. 136–162, 2022, doi: 10.1177/02783649211052067.">.

[15] D. Jones, A. Lewis, and G. S. Fischer, "Development of a standalone surgical haptic arm," in *Proc. IEEE Annu. Int. Conf. Eng. Med. Biol. Soc.*, 2011, pp. 2136–2139.

[16] A. J. Spiers, H. J. Thompson, and A. G. Pipe, "Investigating remote sensor placement for practical haptic sensing with EndoWrist surgical tools," in *Proc. IEEE World Haptics Conf.*, 2015, pp. 152–157.

[17] H. Wang, B. Kang, and D. Y. Lee, "Design of a slave arm of a surgical robot system to estimate the contact force at the tip of the employed instruments," *Adv. Robot.*, vol. 28, no. 19, pp. 1305–1320, Oct. 2014.

[18] T. Ranzani et al., "A novel device for measuring forces in endoluminal procedures," *Int. J. Adv. Robot. Syst.*, vol. 12, no. 8, 2015, Art. no. 116.

[19] S. Kim, C. Kim, S. Park, and D. Y. Lee, "A 3-DOF sensor to estimate the force applied to the tip of a surgical instrument," in *Proc. IEEE 18th Int. Conf. Adv. Robot.*, 2017, pp. 143–148.

[20] G. A. Fontanelli, L. R. Buonocore, F. Ficuciello, L. Villani, and B. Siciliano, "A novel force sensing integrated into the trocar for minimally invasive robotic surgery," in *Proc. IEEE/RSJ Int. Conf. Intell. Robots Syst.*, 2017, pp. 131–136.

[21] A. H. H. Hosseinabadi, M. Honarvar, and S. E. Salcudean, "Optical force sensing in minimally invasive robotic surgery," in *Proc. IEEE Int. Conf. Robot. Automat.*, 2019, pp. 4033–4039.

[22] R. Xue, B. Ren, J. Huang, Z. Yan, and Z. Du, "Design and evaluation of FBG-Based tension sensor in laparoscope surgical robots," *Sensors*, vol. 18, no. 7, pp. 2067:1–2067:18, Jun. 2018.

[23] P. Kazanzides, Z. Chen, A. Deguet, G. S. Fischer, R. H. Taylor, and S. P. DiMaio, "An open-source research kit for the da Vinci surgical system," in *Proc. IEEE Int. Conf. Robot. Automat.*, 2014, pp. 6434–6439.

[24] A. H. H. HadiHosseinabadi and S. E. Salcudean, "UltraLow noise, high bandwidth, low latency, no overload 6-Axis optical force sensor," *IEEE/ASME Trans. Mechatronics*, vol. 26, no. 5, pp. 2581–2592.Oct. 2021.

[25] M. Tavakoli and R. V. Patel, *Haptics in Telerobotic Systems for Minimally Invasive Surgery*. Berlin, Germany: Springer, 2008, pp. 113–124.

[26] AirSealAccess Ports, CONMED - Laparoscopic, Robotic, and Open Surgery, 2021, Accessed: Mar. 10, 2021. [Online]. Available: https://www.conmed.com/en/medical-specialties/laparoscopic-robotic-and-open-surgery/general-and-bariatric-surgery/access/airseal-system/airseal-products/airseal-access-ports